Toward high-frequency operation of spin lasers

Paulo E. Faria Junior,[1,2] Gaofeng Xu,[1] Jeongsu Lee,[1,3] Nils C. Gerhardt,[1,4] Guilherme M. Sipahi,[1,2] and Igor Žutić[1,*]

[1]*Department of Physics, University at Buffalo, State University of New York, Buffalo, New York 14260, USA*

[2]*Instituto de Física de São Carlos, Universidade de São Paulo, 13566-590 São Carlos, São Paulo, Brazil*

[3]*Institute for Theoretical Physics, University of Regensburg, 93040 Regensburg, Germany*

[4]*Photonics and Terahertz Technology, Ruhr-University Bochum, D-44780 Bochum, Germany*

(Received 23 May 2015; published 25 August 2015)

Injecting spin-polarized carriers into semiconductor lasers provides important opportunities to extend what is known about spintronic devices, as well as to overcome many limitations of conventional (spin-unpolarized) lasers. By developing a microscopic model of spin-dependent optical gain derived from an accurate electronic structure in a quantum-well-based laser, we study how its operation properties can be modified by spin-polarized carriers, carrier density, and resonant cavity design. We reveal that by applying a uniaxial strain, it is possible to attain a large birefringence. While such birefringence is viewed as detrimental in conventional lasers, it could enable fast polarization oscillations of the emitted light in spin lasers, which can be exploited for optical communication and high-performance interconnects. The resulting oscillation frequency (>200 GHz) would significantly exceed the frequency range possible in conventional lasers.

DOI: 10.1103/PhysRevB.92.075311 PACS number(s): 42.55.Px, 78.45.+h, 78.67.De, 78.67.Hc

I. INTRODUCTION

Both spin lasers and their conventional (spin-unpolarized) counterparts share three main elements: (i) the active (gain) region, responsible for optical amplification and stimulated emission, (ii) the resonant cavity, and (iii) the pump, which injects (optically or electrically) energy/carriers. The main distinction of spin lasers is a net carrier spin polarization (spin imbalance) in the active region, which, in turn, can lead to crucial changes in their operation, as compared to their conventional counterparts. This spin imbalance is responsible for a circularly polarized emitted light, a result of the conservation of the total angular momentum during electron-hole recombination [1].

The experimental realization of spin lasers [2–19] presents two important opportunities. The lasers provide a path to practical room-temperature spintronic devices with different operating principles, not limited to magnetoresistive effects, which have enabled tremendous advances in magnetically stored information [20–24]. This requires revisiting the common understanding of material parameters for desirable operation [25], as well as a departure from more widely studied spintronic devices, where only one type of carrier (electrons) plays an active role. In contrast, since semiconductor lasers are bipolar devices, a simultaneous description of electrons and holes is crucial.

On the other hand, the interest in spin lasers is not limited to spintronics, as they may extend the limits of what is feasible with conventional semiconductor lasers. It was experimentally demonstrated that injecting spin-polarized carriers already leads to noticeable differences in the steady-state operation [4–6]. The onset of lasing is attained for a smaller injection lasing threshold reduction, while the optical gain differs for different polarizations of light, leading to gain asymmetry, also referred to as gain anisotropy [5,6,8]. In the stimulated emission, even a small carrier polarization in the active region can be greatly amplified and lead to the emission of completely circularly polarized emitted light, an example of a very efficient spin filtering [13].

An intuitive picture for a spin laser is provided by a bucket model in Fig. 1 [26,27]. The uneven water levels represent the spin imbalance in the laser, which implies the following: (i) Lasing threshold reduction—in a partitioned bucket, less water needs to be pumped for it to overfill. There are also two thresholds (for cold and hot water) [28]. (ii) Gain asymmetry—an unequal amount of hot and cold water comes out. A small spin imbalance of pumped carriers can (the two water levels slightly above and below the opening, respectively) result in a complete imbalance in the polarization of the emitted light (here only hot water gushes out) and, consequently, spin-filtering. These effects are attained at room

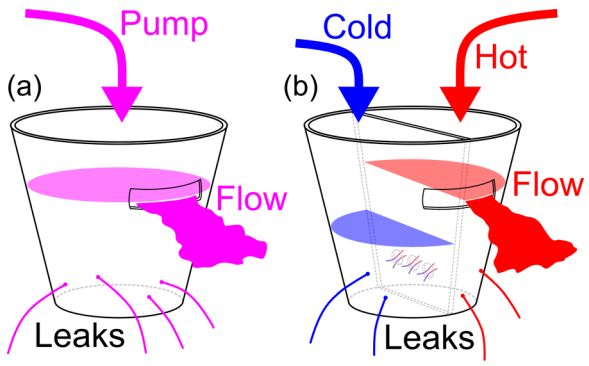

FIG. 1. (Color online) Bucket model for (a) a conventional laser and (b) a spin laser [26]. Water added to the bucket represents the carriers, and the water coming out represents the emitted light. Small leaks depict spontaneous emission, and overflowing water reaching the large opening corresponds to the lasing threshold. In (b) the two halves represent two spin populations (hot and cold water in the analogy), and they are filled separately. The partition between them is not perfect: spin relaxation can cause the two populations to mix. The color code indicates conservation of angular momentum; an unpolarized pumping (violet) is an equal mixture of two polarized contributions (red and blue).

*zigor@buffalo.edu

temperature with either optical or electrical injection. The latter experimental demonstration [17] is a breakthrough toward practical use of spin lasers.

Perhaps the most promising opportunity to overcome the limitations of conventional lasers lies in the dynamic operation of spin lasers, predicted to provide enhanced modulation bandwidth, improved switching properties, and reduced parasitic frequency modulation, i.e., chirp [25,26,29,30]. Moreover, experiments have confirmed that in a given device, a characteristic frequency of polarization oscillations of the emitted light can significantly exceed the corresponding frequency of the intensity oscillations [11,12,16]. This behavior was attributed to birefringence—an anisotropy of the index of refraction, considered detrimental in conventional lasers [31].

What should we then require to attain high-frequency operation in spin lasers? Can we provide guidance for the design of an active region and a choice of the resonant cavity? Unfortunately, to address similar questions, we cannot simply rely on the widely used rate-equation description of spin-lasers [4,5,26,32,33], but instead we need to formulate a microscopic description. The crucial consideration is detailed knowledge of the spectral (energy-resolved) optical gain obtained from an accurate description of the electronic structure in the active region, already important to elucidate a steady-state operation of a spin laser.

A typical vertical geometry, the so-called vertical cavity surface emitting lasers (VCSELs) [31,34–36], used in nearly all spin lasers, is illustrated in Fig. 2(a). Even among conventional lasers, VCSELs are recognized for their unique properties, making them particularly suitable for optical data transmission [36]. The resonant cavity is usually in the range of the emission wavelength, providing a longitudinal single-mode operation. It is formed by a pair of parallel highly reflective mirrors made of distributed Bragg reflectors (DBRs), a layered structure with varying refractive index. The gain active (gain) region usually consists of III-V quantum wells (QWs) or quantum dots (QDs) [7–9,26,37–39].

The key effect of the active region is producing a stimulated emission and coherent light that makes the laser

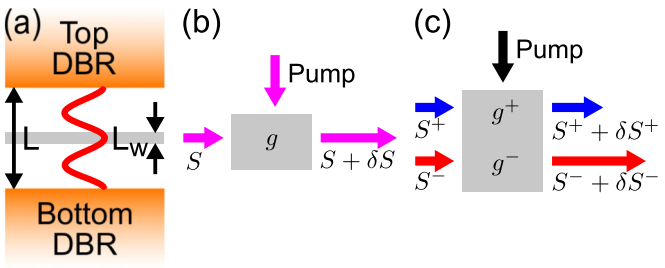

FIG. 2. (Color online) (a) Geometry of a vertical cavity surface-emitting laser. The resonant cavity of length L is formed between the two mirrors made of distributed Bragg reflectors (DBRs). The shaded region represents the active (gain) region of length L_W. The profile of a longitudinal optical mode is sketched. Schematic of the optical gain, g, in the active region for a conventional laser (b) and a spin laser (c). With external pumping/injection, a photon density S increases by δS as it passes across the gain region [40]. In the spin laser, this increase depends on the positive (+)/negative(−) helicity of the light, $S = S^+ + S^-$.

such a unique light source. The corresponding optical gain that describes stimulated emission, under sufficiently strong pumping/injection of carriers, can be illustrated pictorially in Figs. 2(b) and 2(c) for both conventional and spin lasers, respectively. In the latter case, it is convenient to decompose the photon density into different circular polarizations and distinguish that the gain is generally polarization-dependent. If we neglect any losses in the resonant cavity, such a gain would provide an exponential growth rate with the distance across a small segment of gain material [34]. Since both static and dynamic operations of spin lasers depend crucially on their corresponding optical gain, our focus will be to provide its microscopic description derived from an accurate electronic structure of an active region.

After this Introduction, in Sec. II we provide a theoretical framework to calculate the gain in quantum-well-based lasers. In Sec. III, we describe the corresponding electronic structure and the carrier populations under spin injection, the key prerequisites to understanding the spin-dependent gain and its spectral dependence, discussed in Sec. IV. Our gain calculations in Sec. V explain how the steady-state properties of spin lasers can be modified by spin-polarized carriers, carrier density, and resonant cavity design. In Sec. VI, we analyze the influence of a uniaxial strain in the active region, which introduces a large birefringence with the resulting oscillation frequency that would significantly exceed the frequency range possible in conventional lasers. In Sec. VII, we describe various considerations for the optimized design of spin lasers and the prospect of their ultrahigh-frequency operation. A brief summary in Sec. VIII ends our paper.

II. THEORETICAL FRAMEWORK

While both QWs and QDs [7–9] are used for the active region of spin lasers, we focus here on the QW implementation also found in most of the commercial VCSELs [36]. To obtain an accurate electronic structure in the active region, needed to calculate optical gain, we use the $8 \times 8\boldsymbol{k}\cdot\boldsymbol{p}$ method [41]. The total Hamiltonian of the QW system, with the growth axis along the z direction, is

$$H_{\mathrm{QW}}(z) = H_{\boldsymbol{k}\cdot\boldsymbol{p}}(z) + H_{\mathrm{st}}(z) + H_{\mathrm{O}}(z), \tag{1}$$

where $H_{\boldsymbol{k}\cdot\boldsymbol{p}}(z)$ denotes the $\boldsymbol{k}\cdot\boldsymbol{p}$ term, $H_{\mathrm{st}}(z)$ describes the strain term, and $H_{\mathrm{O}}(z)$ includes the band offset at the interface that generates the QW energy profile. The explicit form of these different terms for zinc-blende crystals is given in Appendix A.

Because common nonmagnetic semiconductors are well characterized by the vacuum permeability, μ_0, a complex dielectric function $\varepsilon(\omega) = \varepsilon_r(\omega) + \varepsilon_i(\omega)$, where ω is the photon (angular) frequency, can be used to simply express the dispersion and absorption of electromagnetic waves. The absorption coefficient describing gain or loss of the amplitude of an electromagnetic wave propagating in such a medium is the negative value of the gain coefficient (or gain spectrum) [31,42,43],

$$g^a(\omega) = -\frac{\omega}{cn_r}\epsilon_i^a(\omega), \tag{2}$$

where c is the speed of light, n_r is the dominant real part of the refractive index of the material [42], and $\varepsilon_i^a(\omega)$ is the imaginary

part of the dielectric function, which generally depends on the polarization of light, a, given by

$$\varepsilon_i^a(\omega) = C_0 \sum_{c,v,\vec{k}} \left| p^a_{cv\vec{k}} \right|^2 \left(f_{v\vec{k}} - f_{c\vec{k}}\right) \delta[\hbar\omega_{cv\vec{k}} - \hbar\omega], \quad (3)$$

where the indices c (not to be confused with the speed of light) and v label the conduction and valence subbands, respectively, $\vec{k}$ is the wave vector, $p^a_{cv\vec{k}}$ is the interband dipole transition amplitude, $f_{c(v)\vec{k}}$ is the Fermi-Dirac distribution for the electron occupancy in the conduction (valence) subbands, $\hbar$ is Planck's constant, $\omega_{cv\vec{k}}$ is the interband transition frequency, and δ is the Dirac delta function, which is often replaced to include broadening effects for finite lifetimes [31,44]. The constant C_0 is $C_0 = 4\pi^2 e^2/(\varepsilon_0 m_0^2 \omega^2 \Omega)$, where e is the electron charge, m_0 is the free-electron mass, and Ω is the QW volume.

Analogously to expressing the total photon density in Fig. 2, as the sum of different circular polarizations, $S = S^+ + S^-$, in spin-resolved quantities we use subscripts to describe different spin projections, i.e., eigenvalues of the σ_z Pauli matrix. The total electron/hole density can be written as the sum of the spin-up (+) and spin-down (−) electron/hole densities, $n = n_+ + n_-$ and $p = p_+ + p_-$. In this convention [25,28,29], using the conservation of angular momentum between carriers and photons, the recombination terms are n_+p_+, n_-p_-, while the corresponding polarization of the emitted light depends on the character of the valence-band holes [45]. We can simply define the carrier spin polarization

$$P_\alpha = (\alpha_+ - \alpha_-)/(\alpha_+ + \alpha_-), \quad (4)$$

where $\alpha = n, p$ [46].

Using the dipole selection rules for the spin-conserving interband transitions, the gain spectrum,

$$g^a(\omega) = g^a_+(\omega) + g^a_-(\omega), \quad (5)$$

can be expressed in terms of the contributions of spin-up and -down carriers. To obtain $g^a_{+(-)}(\omega)$, the summation of conduction and valence subbands is restricted to only one spin: $\sum_c \to \sum_{c+(-)}$ and $\sum_v \to \sum_{v+(-)}$ in Eq. (3).

To see how spin-polarized carriers could influence the gain, we show chemical potentials, $\mu_{C(V)}$, for a simplified conduction (valence) band in Fig. 3(a). The spin imbalance in the active region implies that $\mu_{C(V)}$ will also become spin-dependent. Such different chemical potentials lead to the dependence of gain on the polarization of light, described in Fig. 3(b). Without spin-polarized carriers, the gain is the same for S^+ and S^- helicity of light. In an ideal semiconductor laser, $g > 0$ requires a population inversion for photon energies, $E_g < \hbar\omega < (\mu_C - \mu_V)$. However, a gain broadening is inherent to lasers and, as depicted in Fig. 3(b), $g > 0$ even below the band gap, $\hbar\omega < E_g$. If we assume $P_n \neq 0$ [recall Eq. (4)] and $P_p = 0$ (accurately satisfied, as spins of holes relax much faster than electrons), we see different gain curves for S^+ and S^-. The crossover from emission to absorption is now in the range of $(\mu_{C-} - \mu_{V-})$ and $(\mu_{C+} - \mu_{V+})$.

Optical injection of spin-polarized electrons is the most frequently used method to introduce spin imbalance in lasers. Some spin lasers are therefore readily available since they can be based on commercial semiconductor lasers to which a source of circularly polarized light is added subsequently

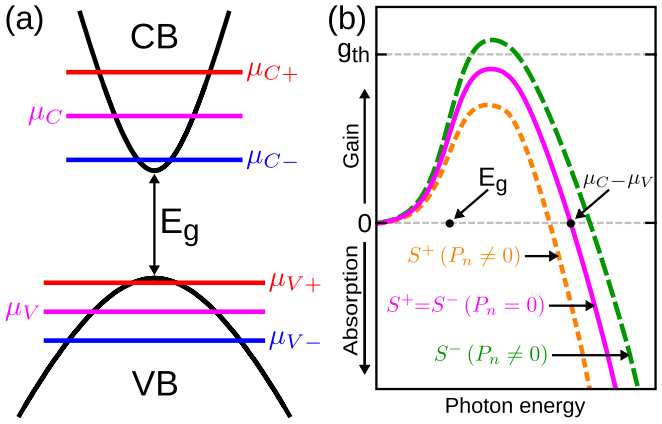

FIG. 3. (Color online) (a) Energy band diagram with a band gap E_g and chemical potentials in conduction (valence) bands, μ_C (μ_V), that in the presence of spin-polarized carriers become spin-dependent: $\mu_{C(V)+} \neq \mu_{C(V)-}$. Unlike the rest of our analysis, here holes are spin-polarized. (b) Gain spectrum for unpolarized (solid) and spin-polarized electrons (dashed curves). Positive gain corresponds to the emission and negative gain to the absorption of photons. The gain threshold g_{th}, required for lasing operation, is attained only for S^- helicity of light.

[4]. Such spin injection can be readily understood from dipole optical selection rules, which apply for both excitation and radiative recombination [1,20].

A simplified band diagram for a zinc-blende QW semiconductor with the corresponding interband transitions is depicted in Fig. 4. At the Brillouin zone center, the valence-band degeneracy of heavy and light holes (HH,LH) in the bulk semiconductor is lifted for QWs due to quantum confinement along the growth direction. The angular momentum

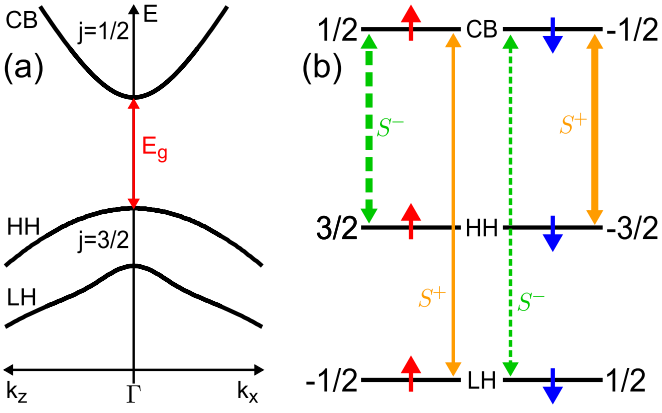

FIG. 4. (Color online) Schematic band structure and optical selection rules in zinc-blende QWs. (a) Conduction band (CB) and valence band with heavy and light holes (HH,LH) labeled by their total angular momentum $j = 1/2$ and $3/2$, representing the states of the orbital angular momentum $l = 0$ and 1, respectively (Appendix A). (b) Interband dipole transitions near the band edge of a QW for light with positive and negative helicity, $S^\pm$, between the sublevels labeled by m_j, the projection of the total angular momentum on the $+z$ axis (along the growth direction). The small arrows represent the projection of spin 1/2 of the orbital part that contributes to the transition, indicating that dipole transitions do not change spin (Appendix B).

of absorbed circularly polarized light is transferred to the semiconductor. Electron orbital momenta are directly oriented by light, and, through spin-orbit interaction, their spins become polarized [1]. While initially holes are also polarized, their spin polarization is quickly lost [20]. Thus, as in Fig. 3(b), we assume throughout this work $P_p = 0$, unless stated otherwise.

The spin polarization of excited electrons depends on the photon energy for S^+ or S^- light. From Fig. 4(b) we can infer that if only CB-HH are involved, $|P_n| \to 1$. At a larger $\hbar\omega$, involving also CB-LH transitions, $|P_n|$ is reduced. Expressing $S^{\pm} \propto Y_1^{\pm 1}$, where Y_l^m is the spherical harmonic, provides a simple connection between dipole selection rules and the conservation of angular momentum in optical transitions (Appendix B).

III. ELECTRONIC STRUCTURE

For our microscopic description of spin lasers, we focus on an (Al,Ga)As/GaAs-based active region, a choice similar to many commercial VCSELs. We consider an $Al_{0.3}Ga_{0.7}As$ barrier and a single 8-nm-thick GaAs QW [47]. The corresponding electronic structure of both the band dispersion and the density of states (DOS) is shown in Fig. 5. Our calculations, based on the $\boldsymbol{k}\cdot\boldsymbol{p}$ method and the 8×8 Hamiltonian from Eq. (1) (Appendix A), yield two confined CB subbands: CB1, CB2, and five VB subbands, labeled in Fig. 5(a) by the dominant component of the total envelope function at $\vec{k} = 0$. The larger number of confined VB subbands stems from larger effective masses for holes than electrons [48]. These differences in the effective masses also appear in the DOS shown in Fig. 5(b).

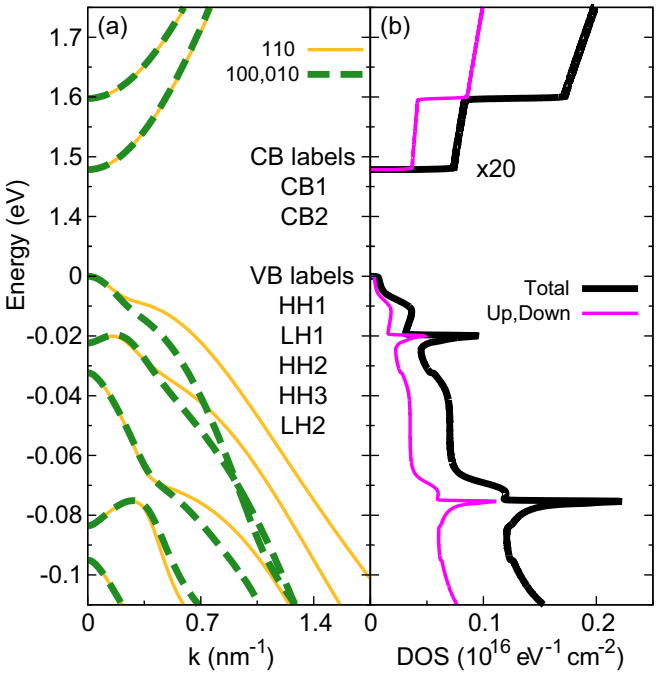

FIG. 5. (Color online) (a) Band structure for the $Al_{0.3}Ga_{0.7}As$/GaAs QW for different k directions along [100], [010], and [110]. (b) DOS calculated from (a). The conduction-band DOS is multiplied by a factor of 20 to match the valence-band scale. The band gap is $E_g = 1.479$ eV (CB1-HH1 energy difference).

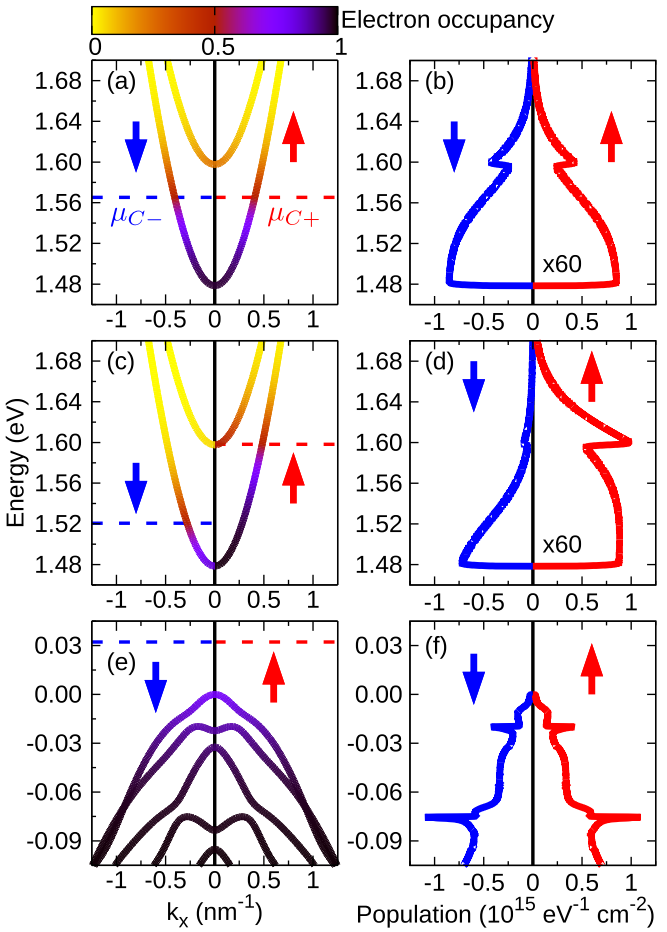

FIG. 6. (Color online) Band structure of Fig. 5(a) with electron occupancy for (a) $P_n = 0$, (c) $P_n = 0.5$, and (e) $P_p = 0$. Carrier population expressed as a product of DOS from Fig. 5(b) and the Fermi-Dirac distribution of electrons for (b) $P_n = 0$, (d) $P_n = 0.5$, and (f) $P_p = 0$. The carrier density is fixed at $n = p = 3 \times 10^{12}$ cm^{-2} and $T = 300$ K. The negative (positive) side of the x axis represents spin-down (-up) electrons, dashed lines denote chemical potentials. The CB population is multiplied by 60 and shown in the same scale as for the VB.

As we seek to describe the gain spectrum in the active region, once we have the electronic structure, it is important to understand the effects associated with carrier occupancies though injection/pumping [recall Fig. 2, Eqs. (2) and (3)]. In Figs. 6(a), 6(c), and 6(e), we show both examples of injected unpolarized ($P_n = 0$) and spin-polarized ($P_n = 0.5$) electrons as seen in the equal and spin-split CB chemical potentials, respectively. The carrier population [34] is given in Figs. 6(b), 6(d), and 6(f) using the product of the Fermi-Dirac distribution and the DOS for CB and VB for both spin projections.

IV. UNDERSTANDING THE SPIN-DEPENDENT GAIN

From the conservation of angular momentum and polarization-dependent optical transitions, we can understand that even in conventional lasers, carrier spin plays a role in determining the gain. However, in the absence of spin-polarized carriers [49], the gain is identical for the two helicities: $g^+ = g^-$, and we recover a simple description (spin- and

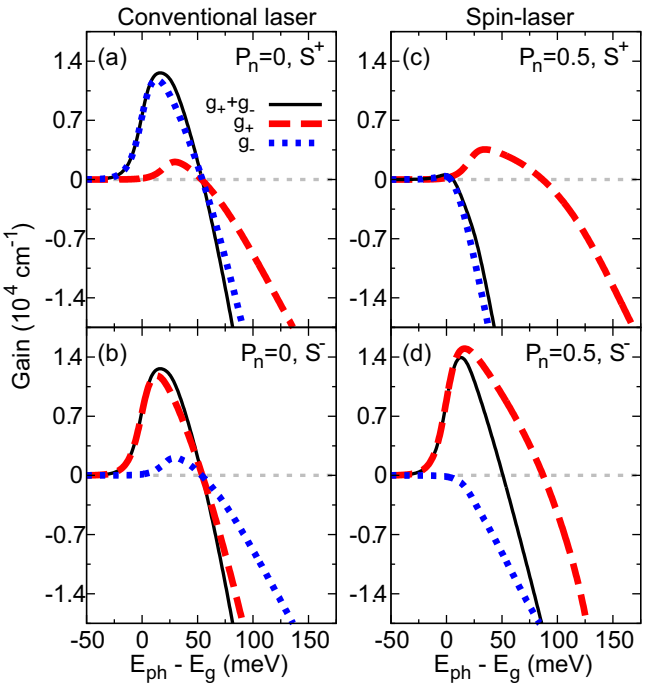

FIG. 7. (Color online) Gain spectra shown as a function of photon energy measured with respect to the energy band gap. Conventional laser, $P_n = 0$ for (a) S^+ and (b) S^- light polarization. Spin-lasers, $P_n = 0.5$ for (c) S^+ and (d) S^- light polarization. The carrier density $n = p = 3 \times 10^{12}$ cm^{-2} and $T = 300$ K are the same as in Fig. 6.

polarization-independent) from Fig. 2(b). In our notation, $g_{\pm}^{\pm}$, the upper (lower) index refers to the circular polarization (carrier spin) [recall Eq. (5)].

This behavior can be further understood from the gain spectrum in Figs. 7(a) and 7(b), where we recognize that $g^+ = g^-$ requires (i) $g_-^+ = g_+^-$ and $g_+^+ = g_-^-$, dominated by CB1-HH1 (1.479 eV $= E_g$) and CB1-LH1 (1.501 eV) transitions, respectively (recall Fig. 5). No spin imbalance implies spin-independent μ_C and μ_V [Fig. 3(a)], and thus $g^{\pm}$, $g_+^{\pm}$, and $g_-^{\pm}$ all vanish the photon energy $E_{ph} = \hbar\omega = \mu_C - \mu_V$. Throughout our calculations, we choose a suitable $\cosh^{-1}$ broadening [44] with a full width at half-maximum (FWHM) of 19.75 meV, which accurately recovers the gain of conventional (Al,Ga)As/GaAs QW systems.

We next turn to the gain spectrum of spin lasers. Why is their output different for S^+ and S^- light, as depicted in Fig. 2(b)? Changing only $P_n = 0.5$ from Figs. 7(a) and 7(b), we see very different results for S^+ and S^- light in Figs. 7(c) and 7(d). $P_n > 0$ implies that $\mu_{C+} > \mu_{C-}$ [see Fig. 6(c)], leading to a larger recombination between the spin-up carriers ($n_+ p_+ > n_- p_-$) and thus to a larger g_+ for S^+ and S^- (red/dashed line) than g_- (blue/dashed line). The combined effect of having spin-polarized carriers and different polarization-dependent optical transitions for spin-up and -down recombination is then responsible for $g^+ \neq g^-$, given by solid lines in Figs. 7(c) and 7(d). For this case, the emitted light S^- exceeds that with the opposite helicity, S^+, and there is a gain asymmetry [5,6,8], another consequence of the polarization-dependent gain. The zero gain is attained at $\mu_{C+} - \mu_V$ for spin-up (red curves) and $\mu_{C-} - \mu_V$ for spin-down transitions (blue curves). The total gain, including both of these contributions, reaches zero at an intermediate value. Without any changes to the band structure, a simple reversal of the carrier spin polarization, $P_n \to -P_n$, reverses the role of preferential light polarization.

V. STEADY-STATE GAIN PROPERTIES

Within our framework, providing spectral information for the gain, we can investigate how the carrier density and its spin polarization, which can be readily modified experimentally, can change the steady-state operation of spin lasers. Specific to VCSELs, it is important to examine how their laser operation is

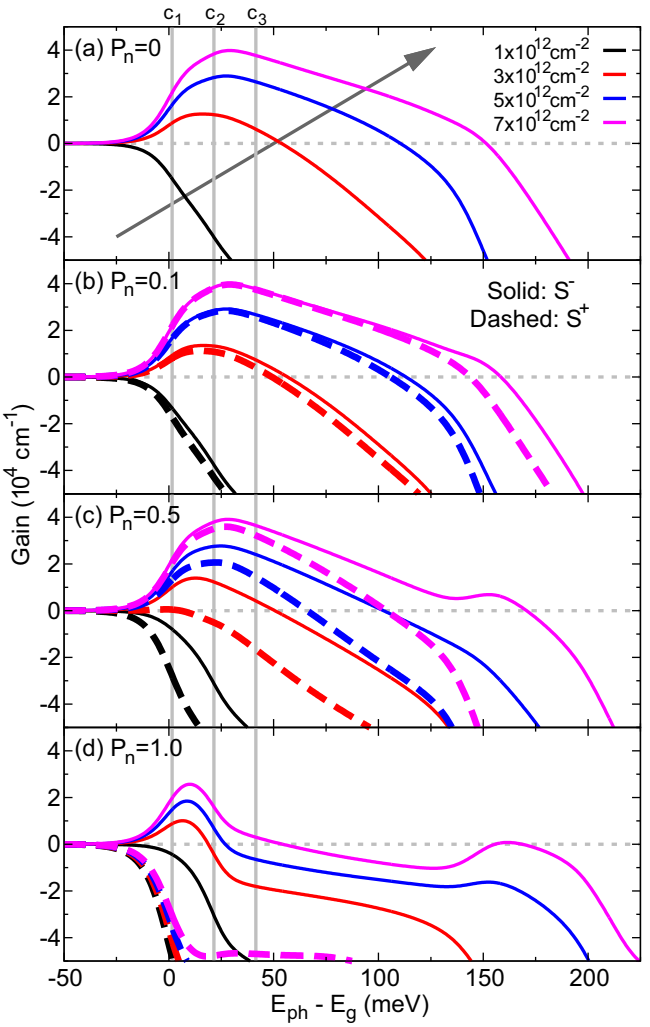

FIG. 8. (Color online) Evolution of the gain spectra with carrier density for (a) $P_n = 0$, (b) $P_n = 0.1$, (c) $P_n = 0.5$, and (d) $P_n = 1.0$. To achieve emission, a certain value of carrier density should be added to the system. The second peak at $E_{ph} - E_g \sim 150$ meV is related to transitions of CB2-HH2. Transitions of CB2-LH2 at $E_{ph} - E_g \sim 200$ meV can be seen in the broader second peak for $P_n = 1.0$. The difference between g^+ and g^- that arises due to spin-polarized carriers in the system increases with P_n. For $P_n = 1.0$ there is no emission of S^+-polarized light, i.e., this component is totally absorbed by the system. The diagonal arrow in Fig. 8 indicates the increase of carrier density in the curves.

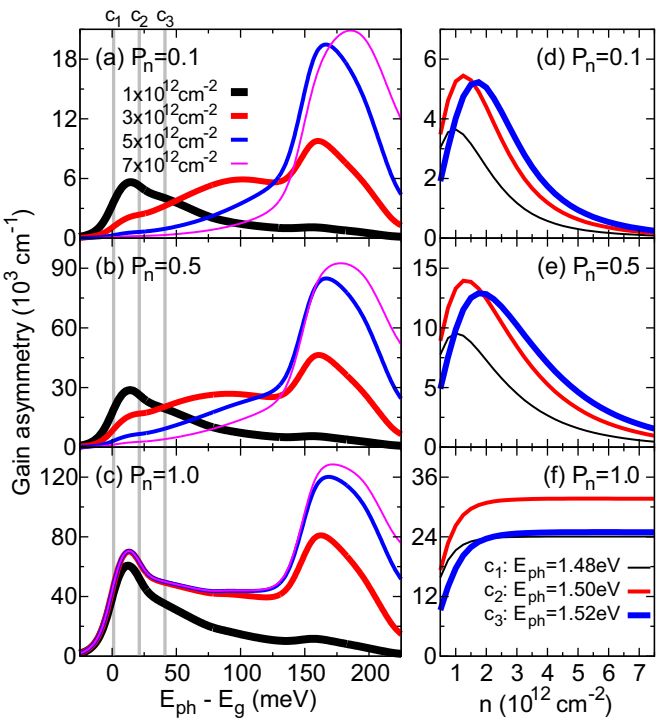

FIG. 9. (Color online) Gain asymmetry obtained from Fig. 8 for (a) $P_n = 0.1$, (b) $P_n = 0.5$, and (c) $P_n = 1.0$. As more carriers are added to the system, the asymmetry peak shifts to higher energies, however this energy region is not necessarily in the regime of a positive gain. Gain asymmetry as a function of carrier density for (d) $P_n = 0.1$, (e) $P_n = 0.5$, and (f) $P_n = 1.0$. Similar to the case of (a)–(c), the asymmetry peaks may not correspond to positive gain.

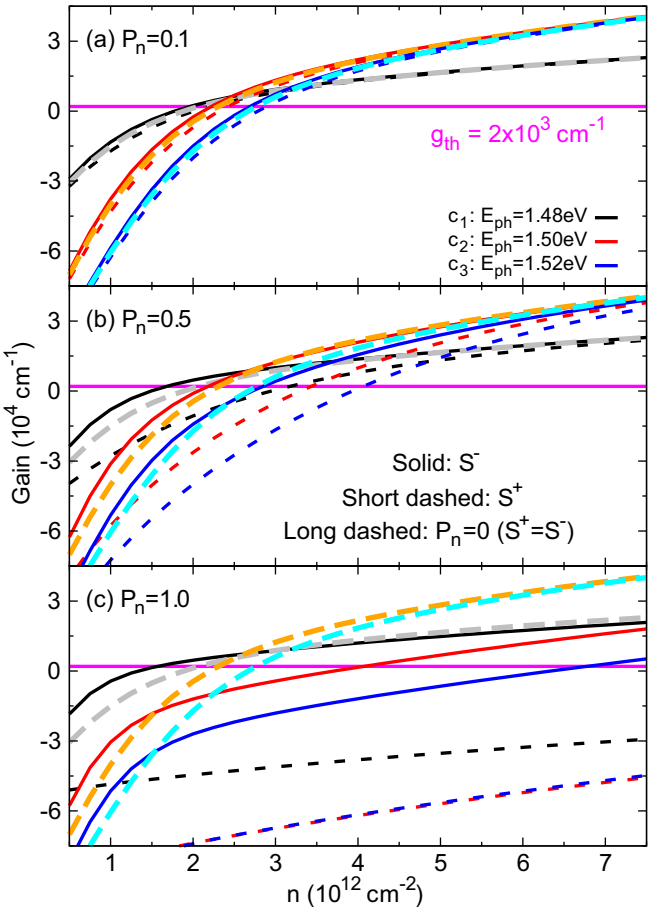

FIG. 10. (Color online) Gain as a function of carrier density for (a) $P_n = 0.1$, (b) $P_n = 0.5$, and (c) $P_n = 1.0$, with the cavity choices c_1, c_2, and c_3. Comparing (i) solid and short-dashed lines, we can examine the spin-filtering effect, and (ii) solid and long-dashed curves, we can examine the threshold reduction. The solid horizontal line indicates the gain threshold, i.e., the losses in the cavity. To achieve the lasing, the value of gain must be greater than the gain threshold.

related to the choice of a resonant cavity, which defines the photon energy at which the constructive interference takes place.

Most of the QW-based lasers do not have a doped active region, and they rely on a charge neutral carrier injection (electrical or optical) [34]. Here we choose $n = p = 1$, 3, 5, and 7×10^{12} cm^{-2}, and spin polarizations $P_n = 0$, 0.1, 0.5, and 1, respectively. Electrical injection in intrinsic III-V QWs using Fe or FeCo allows for $|P_n| \sim 0.3$–0.7 [50–52], while $|P_n| \to 1$ is attainable optically at room temperature [20]. In most of the spin lasers, $|P_n| \lesssim 0.2$ in the active region. We focus on three resonant cavity positions: c_1,c_2,c_3 (vertical lines), defining the corresponding energy of emitted photons $c_1 = 1.48 \sim 1.479$ eV (CB1-HH1 transition), $c_2 = 1.50 \sim 1.501$ eV (CB1-LH1 transition), and $c_3 = 1.52$ eV (at the high-energy side of the gain spectrum).

The corresponding results are given in Fig. 8 showing gain spectra different for S^+ and S^-. This gain asymmetry, $g^+ \neq g^-$, is more pronounced at larger P_n; at $P_n = 1$, there is even no S^+ emission. While this trend is expected and could be intuitively understood, there is a more complicated dependence of the gain asymmetry, $g^-(\hbar\omega) - g^+(\hbar\omega)$, on the carrier density, and the choice of the detuning [42], the energy (frequency) difference between the gain peak, and the resonant cavity position.

The gain asymmetry is one of the key figures of merit for spin lasers, and it can be viewed as crucial for their spin-selective properties, including robust spin-filtering or spin amplification, in which even a small P_n (few percent) in the active region leads to an almost complete polarization of the emitted light (of just one helicity) [13]. Unfortunately, how to enhance the gain asymmetry, beyond just increasing P_n, is largely unexplored.

To establish a more systematic understanding of a gain asymmetry, we closely examine $g^-(\hbar\omega) - g^+(\hbar\omega)$ in Figs. 9(a)–9(c) for different P_n, carrier densities, and resonant cavities. Increasing n, the gain asymmetry peak shifts to higher $\hbar\omega$, indicating an occupation of higher-energy subbands. However, the absolute asymmetry peak is not always in the emission region. For a desirable operation of a spin laser, we should seek a large gain asymmetry with a positive (and a preferably large) gain. Complementary information is given by Figs. 9(d)–9(f) with a density evolution of $g^- - g^+$ for different cavity positions and P_n. Again, we see that the gain asymmetry peak can be attained outside of the lasing region.

The results in Fig. 9 have shown a complex evolution of the gain asymmetry with the cavity position and carrier density. We now repeat a similar analysis for the gain itself in Fig. 10.

The gain calculated for two helicities and unpolarized light ($S^+ = S^-$) provides a useful guide for the threshold reduction and the spin-filtering effect, invoked in a simple bucket model from Fig. 1.

We first consider $P_n = 0.1$, which shows a behavior with an increase in n or, equivalently, an increase in injection, that could be expected from the bucket model. The threshold value of the gain (the onset of an overflowing bucket), g_{th}, is first reached for S^-, then for unpolarized light, a sign of threshold reduction, and finally for S^+ (a subdominant helicity from the conservation of angular momentum and $P_n > 0$). Therefore, there is a spin-filtering interval of n (small, since P_n itself is small) where we expect lasing with only one helicity. A similar behavior appears for all the cavity choices: c_1, c_2, and c_3.

We next turn to $P_n = 0.5$, where c_1 shows trends expected both from the bucket model and early work on spin lasers [4,5]. An increase from $P_n = 0.1$ to 0.5 enhances the threshold reduction and the spin-filtering interval. However, different cavity positions c_2 and c_3 reveal a different behavior. There is a region where unpolarized light $S^+ = S^-$ (long dashed lines) yields a greater gain than for S^- (solid lines). For c_3 the threshold is attained at smaller n for unpolarized light than for negative helicity, i.e., there is no threshold reduction [53]. With $P_n = 1.0$, the threshold reduction is only possible for c_1.

These results reinforce the possibility for a versatile spin-VCSEL design by a careful choice of the resonant cavity, but they also caution that, depending on the given resonant cavity, the usual intuition about the influence of carrier density and spin polarization on the laser operation may not be appropriate.

VI. STRAIN-INDUCED BIREFRINGENCE

An important implication of an anisotropic dielectric function is the phenomenon of birefringence in which the refractive index, and thus the phase velocity of light, depends on the polarization of light [34]. Due to phase anisotropies in the laser cavity [54], the emitted frequencies of linearly polarized light in the x and y directions (S^x and S^y) are usually different. Such birefringence is often undesired for the operation of conventional lasers since it is the origin for the typical complex polarization dynamics and chaotic polarization switching behavior in VCSELs [32,55–58]. While strong values of birefringence are usually considered to be an obstacle for the polarization control in spin-polarized lasers [6,15], the combination of a spin-induced gain asymmetry with birefringence in spin-VCSELs allows us to generate fast and controllable oscillations between S^+ and S^- polarizations [12,16]. The frequency of these polarization oscillations is determined by the linear birefringence in the VCSEL cavity, and it can be much higher than the frequency of relaxation oscillations of the carrier-photon system in conventional VCSELs. This may pave the way toward ultrahigh bandwidth operation for optical communications [12,25,59].

To investigate birefringence effects in the active region of a conventional laser, we consider uniaxial strain by extending the lattice constant in the x direction. For simplicity, we assume the barrier to have the same lattice constant as GaAs, 5.6533 Å, in the y direction. Therefore, both barrier and well regions will have the same extension in the x direction. For $a_x = 5.6544$ Å we have the corresponding element of the strain tensor $\varepsilon_{xx} \sim 0.019\%$, while $a_x = 5.6566$ Å gives $\varepsilon_{xx} \sim 0.058\%$.

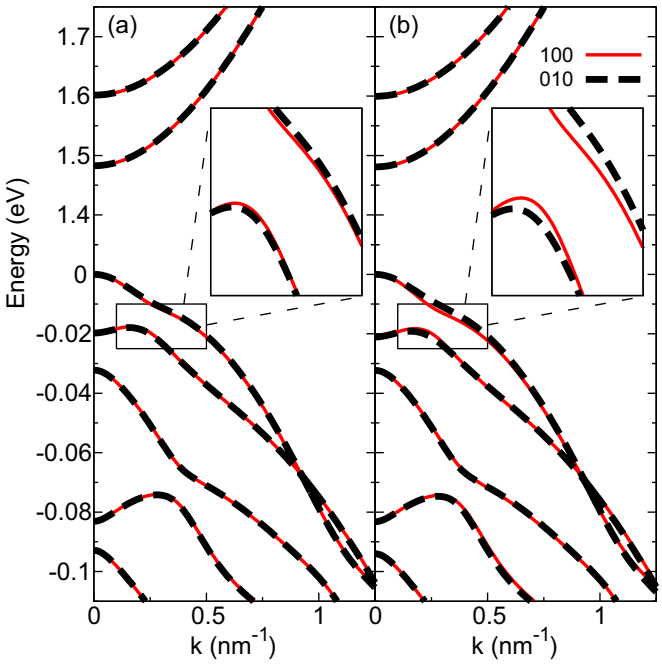

FIG. 11. (Color online) Band structure with uniaxial strain in the active region for (a) $\varepsilon_{xx} \sim 0.019\%$ and (b) $\varepsilon_{xx} \sim 0.058\%$. The inset shows a zoom around the HH1 and LH1 interaction region, where the difference between [100] and [010] directions is more visible. The energy gap of the system is $E_g \sim 1.483$ eV for case (a) and $E_g \sim 1.481$ eV for case (b).

The effect of uniaxial strain in the band structure is presented in Figs. 11(a) and 11(b) for $\varepsilon_{xx} \sim 0.019\%$ and $\varepsilon_{xx} \sim 0.058\%$, respectively. The labeling and ordering of subbands is the same as that in Fig. 5(a). Just this slight anisotropy in the x and y lattice constants creates a difference in subbands for the [100] and [010] directions. In the inset we show the region around the anticrossing of HH1 and LH1 subbands, where the difference is more visible.

In addition to the differences induced in the band structure, the uniaxial strain also induces a change in the dipole selection rules between S^x and S^y light polarizations, which can be seen in the gain spectra we present in Figs. 12(a) and 12(b) for $\varepsilon_{xx} \sim 0.019\%$ and $\varepsilon_{xx} \sim 0.058\%$, respectively. Reflecting the features of the band structure, we notice for the emission region of the gain spectra that the largest difference between g^x and g^y is around the HH1 and LH1 energy regions (between c_1 and c_3 cavity positions, approximately). In the absorption regime (negative gain) we notice $g^x < g^y$, while in the emission regime (positive gain) we have $g^x > g^y$. This feature is more visible in Fig. 12(b).

To calculate the birefringence coefficient in the active region, we used the definition of Ref. [60], given by

$$\gamma_p(\omega) = -\frac{\omega}{2n_e n_g}\delta\varepsilon_r(\omega), \tag{6}$$

where ω is the frequency of the longitudinal mode in the cavity, n_e is the effective index of refraction of the cavity, and n_g is the group refractive index. For simplicity, we assume $n_e = n_g$.

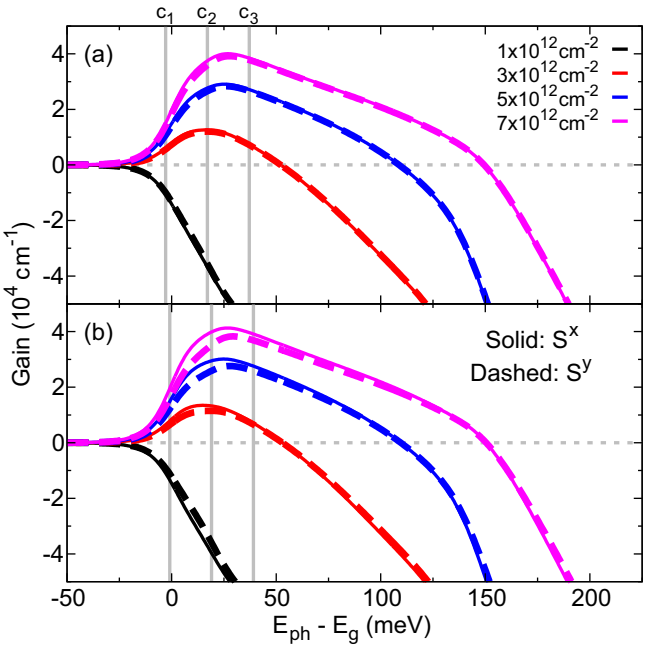

FIG. 12. (Color online) Uniaxial strain modification of gain spectra for strain (a) $\varepsilon_{xx} \sim 0.019\%$ and (b) $\varepsilon_{xx} \sim 0.058\%$. The anisotropy in the lattice constants for the x and y directions modifies the output light polarization of the laser. Since there are no spin-polarized carriers in the system, $g^+ = g^-$.

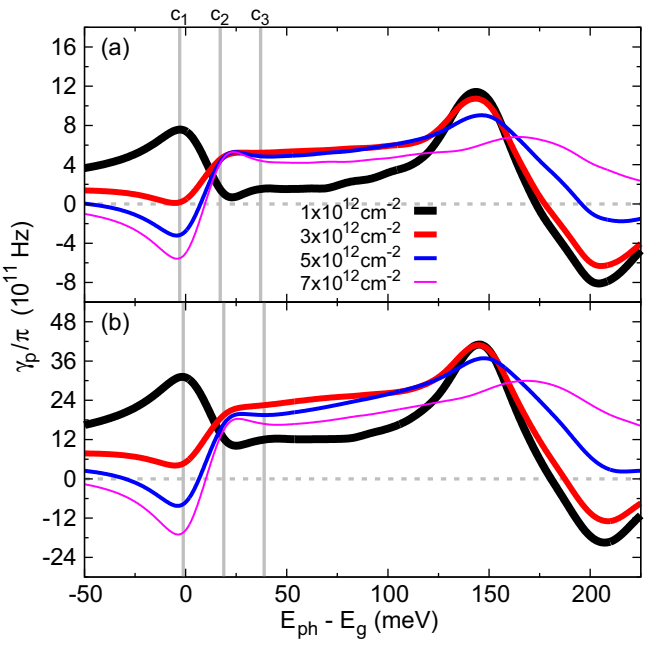

FIG. 13. (Color online) Birefringence coefficient as a function of photon energy considering (a) $\varepsilon_{xx} \sim 0.019\%$ and (b) $\varepsilon_{xx} \sim 0.058\%$. Just an increase of 0.0022 Å in a_x increases γ_p by approximately three times. The two peaks, around $E_{\rm ph} - E_{\rm g} \sim 0$ meV and $E_{\rm ph} - E_{\rm g} \sim 150$ meV, are related to transitions from CB1 and CB2. Transitions related to CB2 are in the absorption regime, not visible in Fig. 12.

The real part of the dielectric function can be obtained from the imaginary part using the Kramers-Kronig relations [42].

We present the birefringence coefficient in Figs. 13(a) and 13(b) for $\varepsilon_{xx} \sim 0.019\%$ and $\varepsilon_{xx} \sim 0.058\%$, respectively. We notice that this strain in the active region, responsible for modest changes in the gain spectra, produces birefringence values of the order of 10^{11}–10^{12} Hz, which may be exploited to generate fast polarization oscillations. Furthermore, when increasing the strain amount by ∼0.04% from case (a) to case (b), the value of γ_p increases approximately threefold [61]. We also included in our calculations spin-polarized electrons, and we notice that they have only a small influence in the birefringence coefficient. Although they change $|g^x|$ and $|g^y|$ slightly, the asymmetry is not affected at all for small spin polarizations of 100%, which are relevant values in real devices.

Investigating the effect of different cavity designs, we present the values of γ_p in Figs. 14(a) and 14(b) for $\varepsilon_{xx} \sim 0.019\%$ and $\varepsilon_{xx} \sim 0.058\%$, respectively. We chose the same photon energies as for the case without birefringence assuming that the different values for the strain-induced birefringence in the active region will not significantly affect the cavity resonance for reasons of simplicity. For the two different strain types, the behavior of γ_p is very similar for the same resonance energy. Comparing different cavity designs, we observe that for c_1, the value of γ_p strongly decreases and also changes sign with the carrier density, n. In contrast, for c_2 and c_3, γ_p is always positive. After a slow increase with n, γ_p becomes flat and nearly independent of the carrier density.

For consistency, we have also calculated the DBR contributions using the approach given by Mulet and Balle [60]. For large anisotropies in the DBR, the birefringence coefficient is on the order of 10^{10} Hz, consistent with the measurements given by van Exter *et al.* [55]. Therefore, for the investigated strain conditions, the main contribution to γ_p comes from the active region, and it is a very versatile parameter that can be fine-tuned using both carrier density and cavity designs, possibly even changing its sign and reaching carrier density-independent regions.

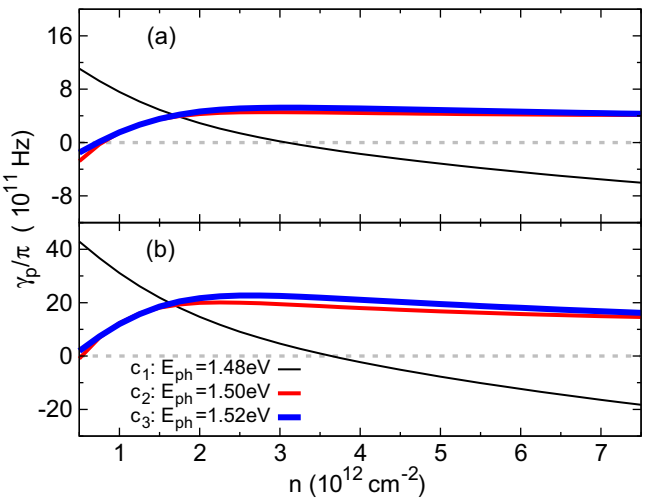

FIG. 14. (Color online) Birefringence coefficient as a function of the carrier density for (a) $\varepsilon_{xx} \sim 0.019\%$ and (b) $\varepsilon_{xx} \sim 0.058\%$. For different cavity designs, the behavior of γ_p can be completely different. The carrier density values where γ_p changes sign in cavity c_1 and the flat region in cavities c_2 and c_3 are already in the lasing regime.

VII. ULTRAHIGH-FREQUENCY OPERATION

Lasers could provide the next generation of parallel optical interconnects and optical information processing [34–36,62–65]. The growth in communication [66] and massive data centers [67] will pose further limitations on interconnects [68]. Conventional metallic interconnects used in multicore microprocessors are increasingly recognized as the bottleneck in maintaining Moore's law scaling and the main source of power dissipation [65,68]. Optical interconnects can effectively address the related limitations, such as the electromagnetic crosstalk and signal distortion, while providing a much larger bandwidth [64,65]. VCSELs are considered particularly suitable for short-haul communication and on-chip interconnects [36]. However, to fully utilize their potential, it would be important to explore the paths for their high-frequency operation and achieve a higher modulation bandwidth, limited for conventional lasers to about ∼50 GHz [36,69].

How can we understand the frequency limitation of a laser? Why would a higher frequency modulation lead to a decrease in a signal-to-noise ratio and limit the effective bandwidth? An accurate analogy is provided by a driven and damped harmonic oscillator. The laser response, just like the harmonic oscillator, is unable to follow a high enough modulation frequency. A Lorentzian-like frequency-dependent displacement of a harmonic oscillator closely matches a modulation response of a laser, decreasing as $1/\omega$, above the corresponding resonance frequency, known as the relaxation oscillation frequency, ω_R, representing a natural oscillation between the carriers and photons and often used to estimate the bandwidth of a laser [34,36,70].

To realize a high-speed operation in conventional lasers requires a careful design and optimization of many parameters. Attaining a high ω_R is closely related to optimizing the gain, which increases with n [71] but decreases with photon density S, known as the gain compression [72], which would be desirable to minimize. For a small-signal modulation $S(t) = S_0 + \delta S(t)$, above the threshold [34],

$$\omega_R^2 \approx v_g(dg/dn)S_0/\tau_{\rm ph}, \tag{7}$$

where v_g is the group velocity of the relevant mode, dg/dn is the differential gain at the threshold, and $\tau_{\rm ph}$ is the photon lifetime. While ω_R increases with S_0, a larger S_0, through gain compression, is detrimental by diminishing the differential gain. There are additional factors, beyond Eq. (7), required for a high ω_R, such as minimizing the transport time for carriers to reach the active region, achieving a high carrier escape rate into the QW barriers, and minimizing extrinsic parasitic effects between the intrinsic laser and the driving circuit [36,70].

Introducing spin-polarized carriers offers additional possibilities to enhance ω_R, corresponding to the modulation of the emitted S, beyond the frequencies attainable in conventional lasers. In the regime of small-signal modulation, both ω_R and the bandwidth have been shown to increase with an increase of the spin polarization of the injected carriers, P_J [26,29], associated with the threshold reduction [thus for a given injection, S_0 is larger than in Eq. (7)]. Similar trends are predicted in the large-signal modulation, but the corresponding increase of ω_R (as compared to the conventional lasers) can exceed what would be expected based only on the threshold reduction due to $P_J \neq 0$ [25].

Another approach to achieve a higher ω_R is to use the polarization dynamics, instead of the intensity dynamics of the emitted light. The coupling between spin-polarized carriers and the light polarization in birefringent microcavities corresponds to different resonant mechanisms than those that govern the light intensity and thus to potentially higher ω_R. Early experiments on polarization dynamics in VCSELs of Oestreich and collaborators have demonstrated spin-carrier dynamics of 120 GHz [73]. However, their (Ga,In)As QW spin lasers operated at 10 K and required a large magnetic field for fast spin precession.

Could we attain similar ultrahigh frequencies at room temperature without an applied magnetic field? Our findings from Sec. VI suggest that indeed such an operation could be realized by a careful design of birefringent cavity properties providing frequency splitting of the two orthogonal linearly polarized lasing modes. While in conventional VCSEL only one linearly polarized mode is emitted, injecting spin-polarized carriers leads to circularly polarized emission and thus the operation of both linearly polarized modes at the same time. The beating between the two frequency-split linearly polarized modes creates polarization oscillations with frequency determined by the birefringence rate, γ_p/π [12,16].

Strain-induced values of γ_p in the active region shown in Figs. 13 and 14 are sufficiently high to exceed the highest available frequency operation of conventional VCSELs. A strong spectral dependence of γ_p, including a possible sign change, requires a careful analysis of the detuning behavior, but it also provides important opportunities for desirable operation of spin-lasers. For example, a large γ_p can be achieved with a very weak dependence on the carrier density. The feasibility of a high-birefringence rate is further corroborated by the experiments using mechanical strain attaining $\gamma_p/\pi \sim 80$ GHz [74], while theoretical calculations suggest even $\gamma_p/\pi \sim$ 400 GHz with asymmetric photonic crystals [75].

VIII. CONCLUSIONS

Our microscopic model of optical gain is based on a similar framework previously employed for conventional lasers [31,34,44] to simply elucidate how introducing spin imbalance could enable their improved dynamical operation. In contrast to the common understanding that the birefringence is detrimental for lasers, we focus on the regime of a large strain-induced birefringence to overcome frequency limitations in conventional lasers.

With a goal to maximize the birefringence-dominated bandwidth in an experimentally realized spin laser, we can use the guidance from the analysis of both high-speed conventional lasers and the steady-state operation of spin lasers to explore potential limiting factors. Future calculations should also examine the influence of a spin-dependent gain compression, Coulomb interactions [44,76,77], an active region with multiple QWs [36], spin relaxation [20,25,78], and a careful analysis of the optimal cavity position that would combine high (differential) gain, high-gain asymmetry, and high γ_p.

While currently the most promising path to demonstrate our predictions for ultrahigh-frequency operation is provided by optically injected spin-polarized carriers to the existing VCSELs, there are encouraging developments for electrically injected spin-polarized carriers. A challenge is to overcome

a relatively large separation between a ferromagnetic spin injector and an active region ($> \mu$m) implying that at 300 K recombining carriers would have only a negligible spin polarization [79]. However, room-temperature electrical injection of spin-polarized carriers has already been realized through spin-filtering by integrating nanomagnets with the active region of a VCSEL [17]. Additional efforts focus on vertical external cavity surface-emitting lasers (VECSELs) [14,15], which could enable a thin-film ferromagnet to be deposited just 100–200 nm away from the active region, sufficiently close to attain a considerable spin polarization of carriers in the active region at room temperature.

Independent progress in spintronics to store and sense information using magnets with a perpendicular anisotropy [80] and to attain fast magnetization reversal [81] could also be directly beneficial for spin lasers. Electrical spin injection usually relies on magnetic thin films with in-plane anisotropy, requiring a large applied magnetic field to achieve an out-of-plane magnetization and the projection of injected spin compatible with the carrier recombination of circularly polarized light in a VCSEL geometry (along the z axis; see Fig. 4). However, a perpendicular anisotropy could provide an elegant spin injection in remanence [82–84], avoiding the technologically undesirable applied magnetic field. The progress in fast magnetization reversal could stimulate implementing all-electrical schemes for spin modulation in lasers that were shown to yield an enhanced bandwidth in lasers [12,16,25,26,29,85,86].

Note added in proof. After this work was completed and submitted, our predictions for high-frequency birefringence were experimentally demonstrated in similar GaAs/AlGaAs quantum well spin VCSELs revealing values of ∼250 GHz [87].

ACKNOWLEDGMENTS

We thank M. R. Hofmann and R. Michalzik for valuable discussions about the feasibility of the proposed spin-lasers and the state-of-the-art active regions in conventional lasers. We thank B. Scharf for carefully reading this manuscript. This work has been supported by CNPq (Grant No. 246549/2012-2), FAPESP (Grants No. 2011/19333-4, No. 2012/05618-0, and No. 2013/23393-8), NSF ECCS-1508873, NSF ECCS-1102092, U.S. ONR N000141310754, NSF DMR-1124601, and the German Research Foundation (DFG) Grant "Ultrafast Spin Lasers for Modulation Frequencies in the 100 GHz Range" GE 1231/2-1.

APPENDIX A

The versatility of the $\boldsymbol{k}\cdot\boldsymbol{p}$ method has been successfully used to obtain the gain spectra in conventional lasers [31,34,35,42,44], as well as to elucidate a wealth of other phenomena, such as the spin Hall effect, topological insulators, and zitterbewegung [88–90]. Our own implementation of the $\boldsymbol{k}\cdot\boldsymbol{p}$ method in this work has been previously tested in calculating the luminescence spectra in δ-doped GaAs [91], confirming experimental and theoretical electronic structure for GaAs QWs [92] and (Al,Ga)N/GaN superlattices [93], identifying fully spin-polarized semiconductor heterostructures, based on (Zn,Co)O [94], and exploring polytypic systems consisting of zinc-blende and wurtzite crystal phases in the same nanostructure [95,96].

Before considering confined systems, it is important to investigate the corresponding bulk crystal structure and construct the functional form of the Hamiltonian. For zinc-blende crystals, the bulk basis set that describes the lower conduction and top valence bands is [20,97–100]

$$
\begin{aligned}
|\mathrm{CB}\Uparrow\rangle &= |S\uparrow\rangle,\\
|\mathrm{CB}\Downarrow\rangle &= |S\downarrow\rangle,\\
|\mathrm{HH}\Uparrow\rangle &= |(X+iY)\uparrow\rangle/\sqrt{2},\\
|\mathrm{LH}\Uparrow\rangle &= i|(X+iY)\downarrow -2Z\uparrow\rangle/\sqrt{6},\\
|\mathrm{LH}\Downarrow\rangle &= |(X-iY)\uparrow +2Z\downarrow\rangle/\sqrt{6},\\
|\mathrm{HH}\Downarrow\rangle &= i|(X-iY)\downarrow\rangle/\sqrt{2},\\
|\mathrm{SO}\Uparrow\rangle &= |(X+iY)\downarrow +Z\uparrow\rangle/\sqrt{3},\\
|\mathrm{SO}\Downarrow\rangle &= i|-(X-iY)\uparrow +Z\downarrow\rangle/\sqrt{3},
\end{aligned}
\tag{A1}
$$

where, compared to Fig. 4(a), we also introduce the spin-orbit spin-split-off subbands $|\mathrm{SO}\rangle$. Here $|S\rangle$ and $|X\rangle,|Y\rangle,|Z\rangle$ are the basis states for irreducible representations $\Gamma_1 \sim x^2+y^2+z^2$ and $\Gamma_{15} \sim x,y,z$, having an orbital angular momentum $l=0$ and 1, respectively. The single arrows ($\uparrow$, $\downarrow$) represent the projection of spin angular momentum $s=1/2$ on the $+z$ axis, while the double arrows ($\Uparrow$, $\Downarrow$) represent the projection of total angular momentum on the $+z$ axis. Rewriting the basis set (A1) in terms of the total angular momentum j and its projection m_j, $|j,m_j\rangle$, we have

$$
\begin{aligned}
|\mathrm{CB}\Uparrow(\Downarrow)\rangle &= |1/2,\,1/2\,(-1/2)\rangle,\\
|\mathrm{HH}\Uparrow(\Downarrow)\rangle &= |3/2,\,3/2\,(-3/2)\rangle,\\
|\mathrm{LH}\Uparrow(\Downarrow)\rangle &= |3/2,\,1/2\,(-1/2)\rangle,\\
|\mathrm{SO}\Uparrow(\Downarrow)\rangle &= |1/2,\,1/2\,(-1/2)\rangle.
\end{aligned}
\tag{A2}
$$

In the basis set of Eq. (A1), the $\boldsymbol{k}\cdot\boldsymbol{p}$ term in Eq. (1) is

$$H_{\boldsymbol{k}\cdot\boldsymbol{p}} = \begin{bmatrix} U & 0 & iP_+ & \sqrt{\frac{2}{3}}P_z & \frac{i}{\sqrt{3}}P_- & 0 & \frac{i}{\sqrt{3}}P_z & \sqrt{\frac{2}{3}}P_- \\ 0 & U & 0 & -\frac{1}{\sqrt{3}}P_+ & i\sqrt{\frac{2}{3}}P_z & -P_- & i\sqrt{\frac{2}{3}}P_+ & -\frac{1}{\sqrt{3}}P_z \\ -iP_- & 0 & Q & S & R & 0 & \frac{i}{\sqrt{2}}S & -i\sqrt{2}R \\ \sqrt{\frac{2}{3}}P_z & -\frac{1}{\sqrt{3}}P_- & S^\dagger & T & 0 & R & -\frac{i}{\sqrt{2}}(Q-T) & i\sqrt{\frac{3}{2}}S \\ -\frac{i}{\sqrt{3}}P_+ & -i\sqrt{\frac{2}{3}}P_z & R^\dagger & 0 & T & -S & -i\sqrt{\frac{3}{2}}S^\dagger & -\frac{i}{\sqrt{2}}(Q-T) \\ 0 & -P_+ & 0 & R^\dagger & -S^\dagger & Q & -i\sqrt{2}R^\dagger & -\frac{i}{\sqrt{2}}S^\dagger \\ -\frac{i}{\sqrt{3}}P_z & -i\sqrt{\frac{2}{3}}P_- & -\frac{i}{\sqrt{2}}S^\dagger & \frac{i}{\sqrt{2}}(Q-T) & i\sqrt{\frac{3}{2}}S & i\sqrt{2}R & \frac{1}{2}(Q+T)-\Delta_{\mathrm{SO}} & 0 \\ \sqrt{\frac{2}{3}}P_+ & -\frac{1}{\sqrt{3}}P_z & i\sqrt{2}R^\dagger & -i\sqrt{\frac{3}{2}}S^\dagger & \frac{i}{\sqrt{2}}(Q-T) & \frac{i}{\sqrt{2}}S & 0 & \frac{1}{2}(Q+T)-\Delta_{\mathrm{SO}} \end{bmatrix}, \tag{A3}$$

with elements

$$\begin{aligned} Q &= -k_x(\tilde{\gamma}_1+\tilde{\gamma}_2)k_x - k_y(\tilde{\gamma}_1+\tilde{\gamma}_2)k_y - k_z(\tilde{\gamma}_1-2\tilde{\gamma}_2)k_z, \\ T &= -k_x(\tilde{\gamma}_1-\tilde{\gamma}_2)k_x - k_y(\tilde{\gamma}_1-\tilde{\gamma}_2)k_y - k_z(\tilde{\gamma}_1+2\tilde{\gamma}_2)k_z, \\ S &= i\sqrt{3}[(k_x\tilde{\gamma}_3k_z + k_z\tilde{\gamma}_3k_x) - i(k_y\tilde{\gamma}_3k_z + k_z\tilde{\gamma}_3k_y)], \\ R &= -\sqrt{3}[(k_x\tilde{\gamma}_2k_x - k_y\tilde{\gamma}_2k_y) - i(k_x\tilde{\gamma}_3k_y + k_y\tilde{\gamma}_3k_x)], \\ U &= E_g + k_xAk_x + k_yAk_y + k_zAk_z, \\ P_\pm &= (1/2\sqrt{2})[P(k_x \pm ik_y) + (k_x \pm ik_y)P], \\ P_z &= (1/2)(Pk_z + k_zP), \end{aligned} \tag{A4}$$

where $\tilde{\gamma}_1$, $\tilde{\gamma}_2$, $\tilde{\gamma}_3$, and A, given in units of $\hbar^2/2m_0$, are the effective-mass parameters of the valence and conduction bands, respectively, explicitly given below. The gap is E_g, the spin-orbit splitting at the Γ point is Δ_{SO}, and P is the Kane parameter of the interband interaction, defined as

$$P = -i\frac{\hbar}{m_0}\langle\alpha|p_l|S\rangle, \tag{A5}$$

with $\alpha = X,Y,Z$ and $l = x,y,z$.

The formulation of a bulk $\boldsymbol{k}\cdot\boldsymbol{p}$ model can vary significantly in its complexity, the choice of the specific system, and the number of bands included. In the description of zinc-blende structures, usually either 6×6 or 8×8 models are employed [98]. In the first case, the information of the valence and conduction band is decoupled, while in the second case their coupling is explicitly included. Their effective-mass parameters are connected by

$$\begin{aligned} \tilde{\gamma}_1 &= \gamma_1 - E_P/3E_g, \\ \tilde{\gamma}_2 &= \gamma_2 - E_P/6E_g, \\ \tilde{\gamma}_3 &= \gamma_3 - E_P/6E_g, \\ A &= \frac{1}{m_e^*} - \left(\frac{E_g + \frac{2}{3}\Delta_{\mathrm{SO}}}{E_g+\Delta_{\mathrm{SO}}}\right)\frac{E_P}{E_g}, \\ E_P &= 2m_0P^2/\hbar^2, \end{aligned} \tag{A6}$$

where $\tilde{\gamma}_{1,2,3}$ are used in the 8×8 model and $\gamma_{1,2,3}$ in the 6×6 model, which can also be related to the tight-binding parameters [92]. To recover the 6×6 model from the 8×8 model, we set $P=0$ in Eqs. (A3), (A4), and (A6).

The strain term, H_{st}, takes a form similar to Eq. (A3) but without the E_g, Δ_{SO}, and P parameters. The matrix elements can be written as

$$\begin{aligned} Q_{\mathrm{st}} &= -a_v(\varepsilon_{xx}+\varepsilon_{yy}+\varepsilon_{zz}) - \frac{b}{2}(\varepsilon_{xx}+\varepsilon_{yy}-2\varepsilon_{zz}), \\ T_{\mathrm{st}} &= -a_v(\varepsilon_{xx}+\varepsilon_{yy}+\varepsilon_{zz}) + \frac{b}{2}(\varepsilon_{xx}+\varepsilon_{yy}-2\varepsilon_{zz}), \\ S_{\mathrm{st}} &= d(\varepsilon_{yz}+i\varepsilon_{xz}), \\ R_{\mathrm{st}} &= -\frac{\sqrt{3}b}{2}(\varepsilon_{xx}-\varepsilon_{yy}) + id\varepsilon_{xy}, \\ U_{\mathrm{st}} &= a_c(\varepsilon_{xx}+\varepsilon_{yy}+\varepsilon_{zz}), \end{aligned} \tag{A7}$$

with a_v, b, and d representing the deformation potentials for the valence band and a_c for the conduction band. The strain tensor components are given by ε_{ij} $(i,j=x,y,z)$.

To treat a QW system, which now lacks translational symmetry along the growth direction, we can replace the exponential part of Bloch's theorem by a generic function. This procedure is called the envelope-function approximation [98], and it leads to the dependence along the growth direction of the $\boldsymbol{k}\cdot\boldsymbol{p}$ and strain parameters in Hamiltonian terms $H_{\boldsymbol{k}\cdot\boldsymbol{p}}(z)$ and $H_{\mathrm{st}}(z)$. Also, the band-offset at the interface of different materials is taken into account in the term $H_{\mathrm{O}}(z)$,

$$H_{\mathrm{O}}(z) = \mathrm{diag}[\delta_V(z),\ldots,\delta_V(z),\delta_C(z),\delta_C(z)], \tag{A8}$$

where $\delta_{V\,(C)}(z)$ describes the energy change in the valence (conduction) band.

Under the envelope-function approximation, the QW Hamiltonian from Eq. (1) is now described by a system of eight coupled differential equations that do not generally have analytical solutions. We solve these equations numerically using the plane-wave expansion for the z-dependent parameters and envelope functions. Details of the envelope-function approximation and plane-wave expansion for QW systems can be found in Refs. [95,96,99].

APPENDIX B

The interband dipole transition amplitude that appears in Eq. (3) is given by

$$p^a_{cv\vec{k}} = \langle c,\vec{k}|\hat{a}\cdot\vec{p}|v,\vec{k}\rangle, \tag{B1}$$

and for the light polarization $S^{\pm}$ we have

$$\hat{a} = \frac{1}{\sqrt{2}}(\hat{x} \pm i\hat{y}), \tag{B2}$$

and therefore

$$\hat{a} \cdot \vec{p} = \frac{p_x \pm ip_y}{\sqrt{2}}. \tag{B3}$$

In the simplified QW of Fig. 4, we are showing the selection rules for $\vec{k} = 0$ and assuming the conduction band as $|c,0\rangle = |\text{CB} \Uparrow (\Downarrow)\rangle$ and the valence band as $|v,0\rangle = |\text{HH} \Uparrow (\Downarrow)\rangle$ or $|v,0\rangle = |\text{LH} \Uparrow (\Downarrow)\rangle$. Calculating the matrix elements between these states, we obtain

$$\langle \text{CB} \Uparrow |p_{\pm}| \text{HH} \Uparrow \rangle = \langle S\uparrow | \frac{p_x \pm ip_y}{\sqrt{2}} \left| \frac{1}{\sqrt{2}}(X + iY) \uparrow \right\rangle = \frac{1}{2}\langle S \uparrow |p_x| X \uparrow \rangle \mp \frac{1}{2}\langle S\uparrow |p_y| Y\uparrow\rangle, \tag{B4}$$

which is nonzero only for p_-,

$$\langle \text{CB} \Downarrow |p_{\pm}| \text{HH} \Downarrow \rangle = \langle S\downarrow | \frac{p_x \pm ip_y}{\sqrt{2}} \left| \frac{i}{\sqrt{2}}(X - iY) \downarrow \right\rangle = \frac{i}{2}\langle S \downarrow |p_x| X \downarrow \rangle \pm \frac{i}{2}\langle S\downarrow |p_y| Y\downarrow\rangle, \tag{B5}$$

which is nonzero only for p_+,

$$\langle \text{CB} \Uparrow |p_{\pm}| \text{LH} \Downarrow \rangle = \langle S\uparrow | \frac{p_x \pm ip_y}{\sqrt{2}} \left| \frac{1}{\sqrt{6}}[(X - iY) \uparrow + 2Z \downarrow] \right\rangle = \frac{1}{2\sqrt{3}}\langle S \uparrow |p_x| X \uparrow \rangle \pm \frac{1}{2\sqrt{3}}\langle S\uparrow |p_y| Y\uparrow\rangle, \tag{B6}$$

which is nonzero only for p_+, and

$$\langle \text{CB} \Downarrow |p_{\pm}| \text{LH} \Uparrow \rangle = \langle S\downarrow | \frac{p_x \pm ip_y}{\sqrt{2}} \left| \frac{i}{\sqrt{6}}[(X + iY) \downarrow - 2Z \uparrow] \right\rangle = \frac{1}{2\sqrt{3}}\langle S \downarrow |p_x| X \downarrow \rangle \mp \frac{1}{2\sqrt{3}}\langle S\downarrow |p_y| Y\downarrow\rangle, \tag{B7}$$

which is nonzero only for p_-.

In addition to Eqs. (B4)–(B7), we can conclude that $\langle \text{CB} \Uparrow |p_{\pm}| \text{HH} \Downarrow \rangle = \langle \text{CB} \Downarrow |p_{\pm}| \text{HH} \Uparrow \rangle = 0$ and $\langle \text{CB} \Uparrow |p_{\pm}| \text{LH} \Uparrow \rangle = \langle \text{CB} \Downarrow |p_{\pm}| \text{LH} \Downarrow \rangle = 0$, independent of the light polarization.

[1] *Optical Orientation*, edited by F. Meier and B. P. Zakharchenya (North-Holland, New York, 1984).

[2] S. Hallstein, J. D. Berger, M. Hilpert, H. C. Schneider, W. W. Rühle, F. Jahnke, S. W. Koch, H. M. Gibbs, G. Khitrova, and M. Oestreich, Phys. Rev. B **56**, R7076 (1997).

[3] H. Ando, T. Sogawa, and H. Gotoh, Appl. Phys. Lett. **73**, 566 (1998).

[4] J. Rudolph, D. Hägele, H. M. Gibbs, G. Khitrova, and M. Oestreich, Appl. Phys. Lett. **82**, 4516 (2003); J. Rudolph, S. Döhrmann, D. Hägele, M. Oestreich, and W. Stolz, *ibid.* **87**, 241117 (2005).

[5] M. Holub, J. Shin, D. Saha, and P. Bhattacharya, Phys. Rev. Lett. **98**, 146603 (2007).

[6] S. Hövel, A. Bischoff, N. C. Gerhardt, M. R. Hofmann, T. Ackemann, A. Kroner, and R. Michalzik, Appl. Phys. Lett. **92**, 041118 (2008).

[7] D. Basu, D. Saha, C. C. Wu, M. Holub, Z. Mi, and P. Bhattacharya, Appl. Phys. Lett. **92**, 091119 (2008).

[8] D. Basu, D. Saha, and P. Bhattacharya, Phys. Rev. Lett. **102**, 093904 (2009).

[9] D. Saha, D. Basu, and P. Bhattacharya, Phys. Rev. B **82**, 205309 (2010).

[10] H. Fujino, S. Koh, S. Iba, T. Fujimoto, and H. Kawaguchi, Appl. Phys. Lett. **94**, 131108 (2009).

[11] M. Li, H. Jähme, H. Soldat, N. C. Gerhardt, M. R. Hofmann, T. Ackemann, A. Kroner, and R. Michalzik, Appl. Phys. Lett. **97**, 191114 (2010).

[12] N. C. Gerhardt, M. Y. Li, H. Jähme, H. Höpfner, T. Ackemann, and M. R. Hofmann, Appl. Phys. Lett. **99**, 151107 (2011).

[13] S. Iba, S. Koh, K. Ikeda, and H. Kawaguchi, Appl. Phys. Lett. **98**, 081113 (2011).

[14] J. Frougier, G. Baili, M. Alouini, I. Sagnes, H. Jaffrès, A. Garnache, C. Deranlot, D. Dolfi, and J.-M. George, Appl. Phys. Lett. **103**, 252402 (2013).

[15] J. Frougier, G. Baili, I. Sagnes, D. Dolfi, J.-M. George, and M. Alouini, Opt. Express **23**, 9573 (2015).

[16] H. Höpfner, M. Lindemann, N. C. Gerhardt, and M. R. Hofmann, Appl. Phys. Lett. **104**, 022409 (2014).

[17] J.-Y. Cheng, T.-M. Wond, C.-W. Chang, C.-Y. Dong, and Y.-F. Chen, Nat. Nanotech. **9**, 845 (2014).

[18] S. S. Alharthi, A. Hurtado, V.-M. Korpijarvi, M. Guina, I. D. Henning, and M. J. Adams, Appl. Phys. Lett. **106**, 021117 (2015).

[19] F.-k. Hsu, W. Xie, Y.-S. Lee, S.-D. Lin, and C.-W. Lai, Phys. Rev. B **91**, 195312 (2015).

[20] I. Žutić, J. Fabian, and S. Das Sarma, Rev. Mod. Phys. **76**, 323 (2004).

[21] J. Fabian, A. Mathos-Abiague, C. Ertler, P. Stano, and I. Žutić, Acta Phys. Slovaca **57**, 565 (2007).

[22] *Handbook of Spin Transport and Magnetism*, edited by E. Y. Tsymbal and I. Žutić (Chapman and Hall/CRC, New York, 2011).

[23] *Spin Dependent Transport in Magnetic Nanostructures*, edited by S. Maekawa, and T. Shinjo (Taylor & Francis, New York, 2002).

[24] S. Das Sarma, J. Fabian, X. D. Hu, and I. Žutić, Superlatt. Microstruct. **27**, 289 (2000).

[25] J. Lee, S. Bearden, E. Wasner, and I. Žutić, Appl. Phys. Lett. **105**, 042411 (2014).

[26] J. Lee, R. Oszwałdowski, C. Gøthgen, and I. Žutić, Phys. Rev. B **85**, 045314 (2012).

[27] I. Žutić and P. E. Faria Junior, Nat. Nanotech. **9**, 750 (2014).

[28] C. Gøthgen, R. Oszwałdowski, A. Petrou, and I. Žutić, Appl. Phys. Lett. **93**, 042513 (2008).

[29] J. Lee, W. Falls, R. Oszwałdowski, and I. Žutić, Appl. Phys. Lett. **97**, 041116 (2010).

[30] G. Boéris, J. Lee, K. Výborný, and I. Žutić, Appl. Phys. Lett. **100**, 121111 (2012).

[31] S. L. Chuang, *Physics of Optoelectronic Devices*, 2nd ed. (Wiley, New York, 2009).

[32] M. San Miguel, Q. Feng, and J. V. Moloney, Phys. Rev. A **52**, 1728 (1995).

[33] A. Gahl, S. Balle, and M. Miguel, IEEE J. Quantum Electron. **35**, 342 (1999).

[34] L. A. Coldren, S. W. Corzine, and M. L. Mašović, *Diode Lasers and Photonic Integrated Circuits*, 2nd ed. (Wiley, Hoboken, NJ, 2012).

[35] S. F. Yu, *Analysis and Design of Vertical Cavity Surface Emitting Lasers* (Wiley, New York, 2003).

[36] *VCSELs Fundamentals, Technology and Applications of Vertical-Cavity Surface-Emitting Lasers*, edited by R. Michalzik (Springer, Berlin, 2013).

[37] R. Oszwałdowski, C. Gøthgen, and I. Žutić, Phys. Rev. B **82**, 085316 (2010).

[38] M. J. Adams and D. Alexandropoulos, IEEE Photon. J. **4**, 1124 (2012).

[39] Spin injection in QDs can even lead to a phonon laser. See, e.g., A. Khaetskii, V. N. Golovach, X. Hu, and I. Žutić, Phys. Rev. Lett. **111**, 186601 (2013).

[40] In a simple picture, neglecting any losses, $dS(z)/dZ = gS(z)$, where z is the coordinate in a small segment of the gain region [34].

[41] Gain calculations for spin-lasers were also performed using the $6 \times 6\boldsymbol{k} \cdot \boldsymbol{p}$ method, which considers the decoupled electronic structure of the conduction and valence bands by M. Holub and B. T. Jonker, Phys. Rev. B **83**, 125309 (2011). The focus was on the steady-state performance of a laser, rather than on the high-frequency operation we consider here.

[42] H. Haug and S. W. Koch, *Quantum Theory of Optical and Electronic Properties of Semiconductors*, 4th ed. (World Scientific, Singapore, 2004).

[43] This gain coefficient corresponds to the ratio of the number of photons emitted per second per unit volume and the number of injected photons per second per unit area, therefore having a dimension of 1/length.

[44] W. W. Chow and S. W. Koch, *Semiconductor-Laser Fundamentals: Physics of the Gain Materials*, (Springer, New York, 1999).

[45] Within the rate-equation description, including a widely used spin-flip model, the $n_+ p_+$ recombination only gives S^- helicity of the emitted light. From the consideration, this means that there is only one type of hole within a four-band model (CB and VB with a twofold spin degeneracy).

[46] Analogous expressions can be introduced for the spin polarization of injection and polarization of photon density.

[47] All bulk, strain, and band-offset parameters were extracted from I. Vurgaftman, J. R. Meyer, and L. R. Ram-Mohan, J. Appl. Phys. **89**, 5815 (2001).

[48] For GaAs, $m_e^* = 0.067$, $m_{\rm hh}^* = 0.350$, $m_{\rm lh}^* = 0.090$, and $m_{\rm so}^* = 0.172$.

[49] We assume that there is no intrinsic magnetic character of the laser due to an applied magnetic field or the presence of a magnetic region.

[50] A. T. Hanbicki, B. T. Jonker, G. Itskos, G. Kioseoglou, and A. Petrou, Appl. Phys. Lett. **80**, 1240 (2002).

[51] T. J. Zega, A. T. Hanbicki, S. C. Erwin, I. Žutić, G. Kioseoglou, C. H. Li, B. T. Jonker, and R. M. Stroud, Phys. Rev. Lett. **96**, 196101 (2006).

[52] G. Salis, R. Wang, X. Jiang, R. M. Shelby, S. S. P. Parkin, S. R. Bank, and J. S. Harris, Appl. Phys. Lett. **87**, 262503 (2005).

[53] The possibility for an increase in threshold in spin lasers with $P_n = 1$ has been predicted in Ref. [41]. However, we show that such an increase is not universal and depends on the cavity choice, i.e., the detuning between the cavity mode and the gain peak.

[54] A simple phase condition for the standing-wave pattern [recall Fig. 2(a)] can be written as $L = m\lambda/(2n)$ [36], where L is the cavity length, m is the mode index, and λ is the wavelength of the emitted light. The polarization dependence of the refractive index, n, thus leads to the polarization dependence of the emitted frequency.

[55] M. P. van Exter, A. K. Jansen van Doorn, and J. P. Woerdman, Phys. Rev. A **56**, 845 (1997).

[56] M. Sondermann, M. Weinkath, and T. Ackemann, IEEE J. Quantum Electron. **40**, 97 (2004).

[57] M. Virte, K. Panajotov, H. Thienpont, and M. Sciamanna, Nat. Photon. **7**, 60 (2012).

[58] R. Al-Seyab, D. Alexandropoulos, I. D. Henning, and M. J. Adams, IEEE Photon. J. **3**, 799 (2011).

[59] N. C. Gerhardt and M. R. Hofmann, Adv. Opt. Technol. **2012**, 268949 (2012).

[60] J. Mulet and S. Balle, IEEE J. Quantum Electron. **38**, 291 (2002).

[61] The birefringence coefficient in a VCSEL can also be enhanced by local heating. A. K. Jansen van Doorn, M. P. van Exter, and J. P. Woerdman, IEEE J. Quantum Electron. **34**, 700 (1998).

[62] *Optical Fiber Telecommunications VIA Components and Subsystems*, 6th ed., edited by I. P. Kaminow, T. Li, and A. E. Willner (Academic, New York, 2013).

[63] G. P. Agrawal, *Fiber-Optic Communication Systems*, 3rd ed. (Wiley, New York, 2002).

[64] B. Ciftcioglu, R. Berman, S. Wang, J. Hu, I. Savidis, M. Jain, D. Moore, M. Huang, E. G. Friedman, G. Wicks, and H. Wu, Opt. Express **20**, 4331 (2012).

[65] D. A. B. Miller, Proc. IEEE **97**, 1166 (2009).
[66] M. Hilbert and P. López, Science **332**, 60 (2011).
[67] Scalable, energy-efficient data centers and clouds, 2012, Santa Barbara, CA, http://iee.ucsb.edu/files/Institute for Energy Efficiency Data Center Report.pdf.
[68] www.itrs.net/Links/2011ITRS/2011Chapters/2011Interconnect.pdf.
[69] P. Westbergh, E. P. Haglund, E. Haglund, R. Safaisini, J. S. Gustavsson, and A. Larsson, Electron. Lett. **49**, 1021 (2013).
[70] *Semiconductor Lasers I*, edited by E. Kapon (Academic, San Diego, 1999).
[71] We assume a typical description of an active region that is usually undoped and has a charge neutrality, $n = p$.
[72] Attributed to the spectral hole burning and carrier heating effects in Ref. [70].
[73] M. Oestreich, J. Hübner, D. Hägele, M. Bender, N. Gerhardt, M. Hofmann, W. W. Rühle, H. Kalt, T. Hartmann, P. Klar, W. Heimbrodt, and W. Stolz, *Spintronics: Spin Electronics and Optoelectronics in Semiconductors*, in Advances in Solid State Physics Vol. 41, edited by B. Kramer (Springer, Berlin, 2001), pp. 173–186.
[74] K. Panajotov, B. Nagler, G. Verschaffelt, A. Georgievski, H. Thienpont, J. Danckaert, and I. Veretennicoff, Appl. Phys. Lett. **77**, 1590 (2000).
[75] M. Dems, T. Czyszanowski, H. Thienpont, and K. Panajotov, Opt. Commun. **281**, 3149 (2008).
[76] D. Burak, J. V. Moloney, and R. Binder, Phys. Rev. A **61**, 053809 (2000).
[77] G. D. Sanders, C.-K. Sun, B. Golubovic, J. G. Fujimoto, and C. J. Stanton, Phys. Rev. B **54**, 8005 (1996).
[78] I. Žutić, J. Fabian, and S. Das Sarma, Appl. Phys. Lett. **82**, 22 (2003).
[79] H. Soldat, M. Y. Li, N. C. Gerhardt, M. R. Hofmann, A. Ludwig, A. Ebbing, D. Reuter, A. D. Wieck, F. Stromberg, W. Keune, and H. Wende, Appl. Phys. Lett. **99**, 051102 (2011).
[80] Commercial magnetic hard drives already employ ferromagnets with perpendicular anisotropy, which enables a higher information density to be stored.
[81] S. Garzon, L. Ye, R. A. Webb, T. M. Crawford, M. Covington, and S. Kaka, Phys. Rev. B **78**, 180401(R) (2008).
[82] A. Sinsarp, T. Manago, F. Takano, and H. Akinaga, Jpn. J. Appl. Phys. **46**, L4 (2007).
[83] S. Hövel, N. C. Gerhardt, M. R. Hofmann, F.-Y. Lo, A. Ludwig, D. Reuter, A. D. Wieck, E. Schuster, H. Wende, W. Keune, O. Petracic, and K. Westerholt, Appl. Phys. Lett. **93**, 021117 (2008).
[84] J. Zarpellon, H. Jaffres, J. Frougier, C. Deranlot, J. M. George, D. H. Mosca, A. Lemaitre, F. Freimuth, Q. H. Duong, P. Renucci, and X. Marie, Phys. Rev. B **86**, 205314 (2012).
[85] D. Banerjee, R. Adari, M. Murthy, P. Suggisetti, S. Ganguly, and D. Saha, J. Appl. Phys. **109**, 07C317 (2011).
[86] There is also an encouraging progress in light-emitting diodes showing electrical helicity switching. N. Nishizawa, K. Nishibayashi, and H. Munekata, Appl. Phys. Lett. **104**, 111102 (2014).
[87] T. Pusch, M. Lindemann, N. C. Gerhardt, M. R. Hofmann, and R. Michalzik, Electron. Lett. (to be published).
[88] S. Murakami, N. Nagaosa, and S.-C. Zhang, Science **301**, 1348 (2003).
[89] M. Z. Hasan and C. L. Kane, Rev. Mod. Phys. **82**, 3045 (2010).
[90] E. Bernardes, J. Schliemann, M. Lee, J. C. Egues, and D. Loss, Phys. Rev. Lett. **99**, 076603 (2007).
[91] G. M. Sipahi, R. Enderlein, L. M. R. Scolfaro, J. R. Leite, E. C. F. da Silva, and A. Levine, Phys. Rev. B **57**, 9168 (1998).
[92] J. Lee, K. Výborný, J. E. Han, and I. Žutić, Phys. Rev. B **89**, 045315 (2014).
[93] S. C. P. Rodrigues, L. M. R. Scolfaro, J. R. Leite, and G. M. Sipahi, Appl. Phys. Lett. **76**, 1015 (2000).
[94] I. S. P. Marin, G. M. Sipahi, M. A. Boselli, and I. C. da Cunha Lima, Appl. Phys. Lett. **89**, 192101 (2006).
[95] P. E. Faria Junior and G. M. Sipahi, J. Appl. Phys. **112**, 103716 (2012).
[96] P. E. Faria Junior, T. Campos, and G. M. Sipahi, J. Appl. Phys. **116**, 193501 (2014).
[97] R. Enderlein and N. J. Horing, *Fundamentals of Semiconductor Physics and Devices*, 1st ed. (World Scientific, Singapore 1997).
[98] R. Winkler, *Spin-orbit Coupling Effects in Two-Dimensional Electron and Hole Systems* (Springer, New York, 2003).
[99] G. M. Sipahi, R. Enderlein, L. M. R. Scolfaro, and J. R. Leite, Phys. Rev. B **53**, 9930 (1996).
[100] R. Enderlein, G. M. Sipahi, L. M. R. Scolfaro, and J. R. Leite, Phys. Rev. Lett. **79**, 3712 (1997).